Activation of Oxygen-Stabilized Sulfur for Li and Na Batteries

Chao Luo, Yujie Zhu, Oleg Borodin, Tao Gao, Xiulin Fan, Yunhua Xu, Kang Xu, and Chunsheng Wang**

The sulfur-based cathode materials suffer severely from poor cycling stability and low utilization, incurred by their stepwise reaction mechanism that generates polysulfide intermediates and the subsequent irreversible losses. In this work, those issues are significantly relieved by entrapping sulfur species in carbon host rich in oxygen functionalities. Sulfur species in such C/S composite are highly stabilized by their interaction with oxygen, and can deliver a reversible capacity of 508 mAh/(g of S) for 2000 cycles when coupled with Li, representing the best cycling stability up to date. More interestingly, extra capacity can be accessed by simply prelithiating the oxygen-stabilized C/S composites down to 0.6 V for a few cycles, which enables a high capacity of 1621 mAh/(g of S) that eventually stabilizes at 820 mAh/(g of S) for 600 cycles. The mechanism for this electrochemical activation process is investigated with both spectroscopic and electrochemical techniques, which reveal that the inactive sulfur bonded to oxygen is liberated in the initial deep lithiation precycles and becomes electrochemically active. The oxygen-stabilized sulfur can also be coupled with Na anode to form Na/S cell, confirming that the formation of S–O interaction in C/S composite generates promising sulfur-based cathode materials for Li–S and Na–S batteries.

1. Introduction

Li-ion batteries have been widely used to power the portable electronics. However, their penetration into the markets of vehicular electrification and grid-storage has been hindered by their moderate energy densities,[1,2] since the intercalation-type cathode materials in state-of-the-art Li-ion batteries impose an intrinsic limit on device energy density.[3–5] Even though lithium rich metal oxides have been demonstrated to deliver the highest capacity (≈250 mAh g^{-1})[6,7] among all transition metal oxide materials, their structural stability over the long-term cycling still presents challenges to practical applications, so does their compatibility with the state-of-the-art anode materials such as Si- and Sn-based alloys.[8–10]

At present, the most promising alternative cathode material is sulfur due to its high theoretical capacity (1672 mAh g^{-1}), low cost, high abundance in nature, and environmental benignity.[11–13] However, the rechargeable battery chemistry based on sulfur cathode still faces three intrinsic challenges:[14–19] (1) the formation of intermediate polysulfide products and the parasitic shuttle reaction caused by them during lithiation/delithiation process, resulting in low Coulombic efficiency and rapid capacity fading; (2) the extremely low electronic and ionic conductivities of both starting material S and ending product Li_2S, which are responsible for not only low capacity utilization but also poor power density; and (3) the stress/strain induced by the large volume difference (76%) between sulfur (2.03 g cm^{-3}) and Li_2S (1.66 g cm^{-3}) during a complete lithiation/delithiation cycle, which destroys the physical integrity of sulfur cathode and results in fast capacity loss. Significant efforts have been made to address these challenges, the most popular of which is to entrap sulfur into electronic conductive hosts of nanostructures, such as microporous carbon, carbon nanotube, graphene, graphene oxide, and carbon nanofiber;[20–32] nevertheless, commercialization of sulfur cathode remains remote. In fact, since these three challenges are closely entangled, it is difficult to circumvent all of them with a single strategy. For example, adoption of electrolytes with high solubility for high-order polysulfide effectively relieved the poor conductivity issue and reduced the stress/strain,[33] but it also accelerated the parasitic shuttle reaction, while the sulfur–TiO_2 yolk–shell nanoarchitecture with internal void space successfully accommodated the volume expansion of sulfur,[17] but the lower electronic conductivity of TiO_2-host further worsened the utilization and reaction kinetics of S-TiO_2. Carbon coating on Li_2S mitigated the stress/strain and the loss of active species due to the physical disintegration of the electrode, but the large particle size (500 nm–2 µm) of Li_2S reduced the utilization.[34]

C. Luo, Dr. Y. Zhu, T. Gao, Dr. X. Fan, Dr. Y. Xu, Prof. C. Wang
Department of Chemical and Biomolecular Engineering
University of Maryland
College Park, MD 20742, USA
E-mail: cswang@umd.edu
Dr. O. Borodin, Dr. K. Xu
Electrochemistry Branch
Army Research Laboratory
Adelphi, MD 20783, USA
E-mail: conrad.k.xu.civ@mail.mil

DOI: 10.1002/adfm.201503918

In this work, oxygen-stabilized sulfur in carbon matrix was formed in situ by heating sulfur in a sealed vacuum glass tube at 600 °C with 3,4,9,10-perylentetracarboxylic dianhydrid (PTCDA), an aromatic compound with the composition of minimum hydrogen, moderate oxygen but rich carbon ($C_{24}H_8O_6$), makes it an ideal precursor for carbon. The carbonization of PTCDA ensures the formation of a carbonaceous matrix that is characterized of oxygen functionalities that might either covalently or Coulombically bonded to sulfur species. The transmission electron microscopy (TEM), X-ray diffraction (XRD), X-ray photoelectron spectroscopy (XPS), and Raman characterizations reveal that sulfur is uniformly immobilized in the carbon host at nano or even at molecular level, which should reduce the parasitic shuttle reactions incurred by unattached sulfur species and their intermediate reduction products. A portion of sulfur is strongly interacted with oxygen functionalities in the carbon, which is inactive during normal charge/discharge cycles between 1.0 and 3.0 V, the unbounded sulfur in the carbon provided a reversible capacity of 508 mAh/(g of S) for 2000 cycles with an average loss of 0.0045% per cycle in carbonate-based electrolyte, which is lower than the best record by an order of magnitude.

This excellent cycling stability, however, was realized at the expense of capacity utilization, because the 508 mAh/(g of S) only represents a small portion of S accessed by the cell reaction. To liberate electrochemically inactive S species that strongly interacted with oxygen-functionalities, we reduced the lithiation potential down to 0.60 V for several cycles before normal charge/discharge cycling between 1.0 and 3.0 V started, and achieved in the subsequent cycles a remarkably high capacity of 1621 mAh/(g of S), which is close to the theoretical value of sulfur (1672 mAh g^{-1}). In the following long-term cycling, an effective capacity of 820 mAh/(g of S) was maintained for 600 cycles between 1.0 and 3.0 V.

2. Results and Discussion

2.1. Material Characterization

The neat PTCDA carbonized with and without sulfur are characterized by scanning electron microscopy (SEM) and TEM, respectively, as shown in **Figure 1**. The carbonized PTCDA consists of elongated rectangular plates with a length about 20 μm and a width about 4 μm. Uniform wrinkles can be observed on the surface of the plates. However, C/S composites formed by *in situ* annealing the mixture of PTCDA and sulfur are revealed to be porous spheres with diameter around 15–20 μm, which consist of aggregated secondary short plates with a diameter of ≈500 nm. The drastically different morphology, because of the introduction of sulfur, indicates that possible chemical interactions are formed between the carbonized PTCDA host and the S guest.

The distribution of carbon, sulfur, and oxygen in a secondary C/S particle (Figure 1c) was analyzed using energy dispersive X-ray spectroscopy (EDS), as shown in Figure 1d–f, in which carbon homogenously overlaps with sulfur and oxygen, suggesting a uniform distribution of carbon, sulfur, and oxygen throughout the composite. The chemical composition of the composite was determined using the elemental analysis to be 56% of carbon, 38% of sulfur, and 5% of oxygen, while thermogravimetric analysis (TGA) was also used to determine sulfur-content, which indicates that there is only 8% weight loss after heating up to 600 °C as shown in Figure S1 (Supporting Information), much lower than the sulfur content determined by the elemental analysis. Since TGA actually only detects the sulfur species that are simply chemisorbed in micropores and can be evaporated due to heat, the extra sulfur-content, as determined by elemental analysis, should reflect the fact that a substantial amount of sulfur in the C/S composite may be chemically bonded to the oxygen-functionalities (5%) in carbonaceous host via either covalent or ionic interactions.

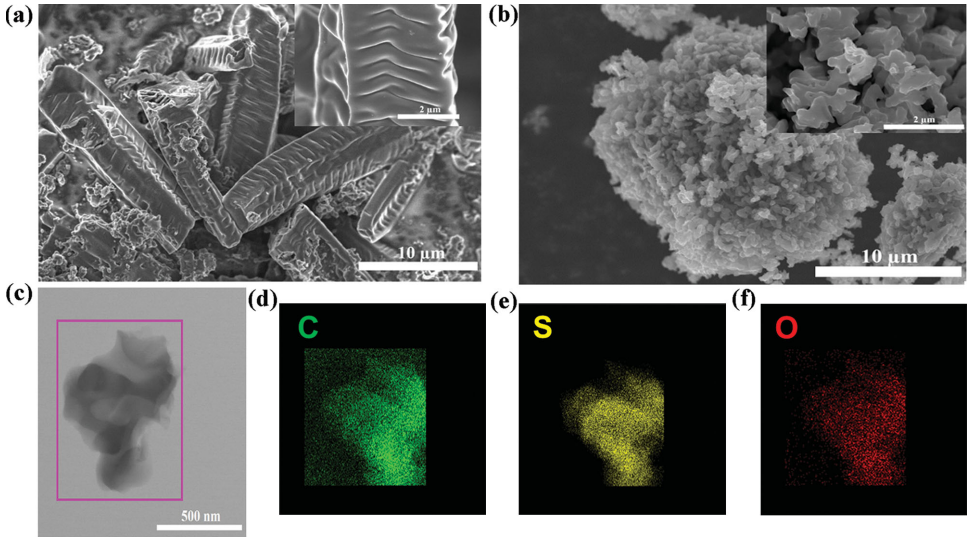

Figure 1. SEM images of a) carbonized PTCDA and b) oxygen-stabilized C/S composites; c) TEM image of oxygen-stabilized C/S composites: elemental mapping images of the C/S composite: d) carbon, e) sulfur, and f) oxygen.

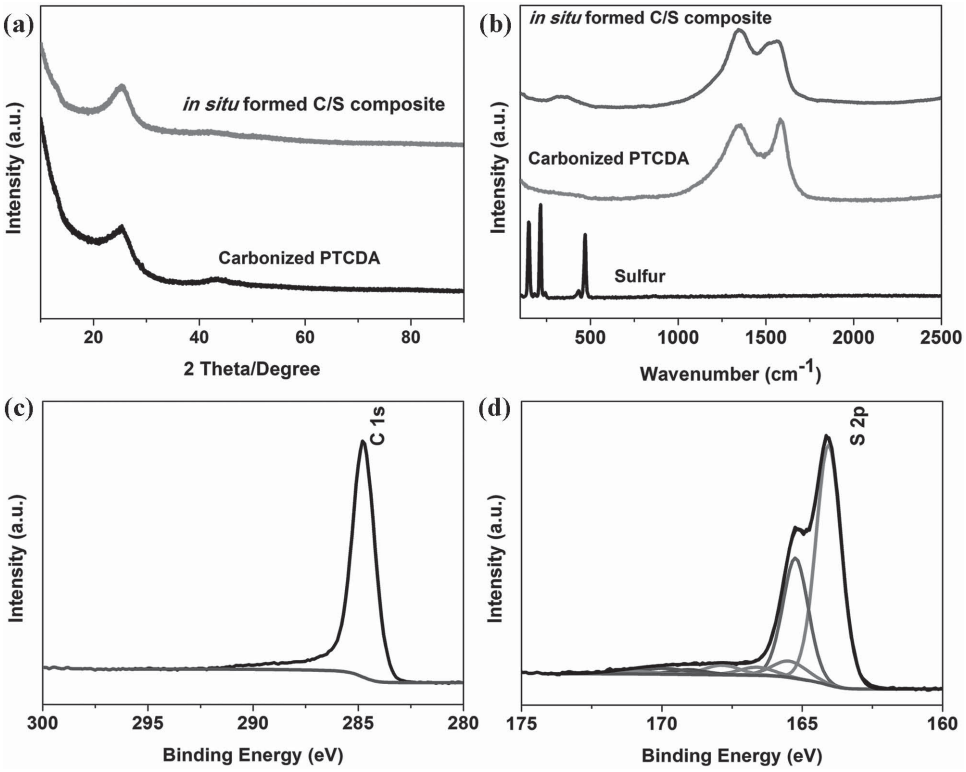

Figure 2. a) XRD patterns and b) Raman spectra for pristine S, carbonized neat PTCDA, and oxygen-stabilized C/S composites; XPS spectra of oxygen stabilized C/S composites: c) C 1s, d) S 2p.

The nature of bonding between oxygen and sulfur in C/S composites is further characterized by XRD, Raman spectroscopy, and XPS (**Figure 2**). The carbonized neat PTCDA and oxygen-stabilized C/S composites show similar XRD patterns (Figure 2a), where a broad peak at 26° indicates the existence of graphitic carbon in both samples. No sulfur peak is observed in C/S composites, suggesting that sulfur species fails to crystallize and remains in the amorphous form, perhaps due to the strong interaction with O-functionalities. Raman spectra of carbonized neat PTCDA and oxygen-stabilized C/S composites in Figure 2b show two broad peaks at 1345 and 1595 cm^{-1}, respectively, confirming the coexistence of disordered graphite (D band) and crystalline graphite (G band). The valence states of sulfur in the composite could be determined from high resolution XPS, as shown in Figure 2c,d, where elemental C 1s at 284.8 eV was used as reference binding energy. The asymmetry of C 1s spectra demonstrates the presence of both sp^2 and sp^3 carbon, which are ascribed to graphitic carbon and amorphous carbon in the composite, respectively. A host of peaks corresponding to the S 2p spectra are detected between 164 and 170 eV, among which the twin peaks located at 164.0 and 165.2 eV should be attributed to the S $2p_{3/2}$ and S $2p_{1/2}$ of sulfur species containing S–S bond, probably arising from short-chain S_x ($x \leq 8$), while a host of small peaks at higher binding energies starting from 165.5 eV should arise from sulfur in strong interaction with oxygen in varying manners (S–O, S=O, etc.), which were results of the reaction between sulfur and oxygen functionalities in PTCDA. The Brunauer–Emmett–Teller (BET) analysis (Figure S2, Supporting Information) revealed that C/S composite thus made has a dense structure with a surface area of 23.4227 $m^2\ g^{-1}$. From the shape of N_2 adsorption/desorption isotherms and pore-size distribution, one can conclude that the composite is not a porous structure, which might suggest that sulfur filled the micropores of carbon host and is tightly bonded to the carbon matrix.

2.2. Electrochemical Performance

The electrochemical performances of oxygen-stabilized C/S composites are evaluated in coin cells with Li metal as anode. **Figure 3**a shows their galvanostatic voltage profiles when cycled between 1.0 and 3.0 V. In the first cycle, a short plateau at 2.4 V represents the reduction of S_x to Li_2S_x, followed by a long plateau at 1.6 V corresponding to further reduction of shorter S chains to Li_2S_2/Li_2S. During the delithiation a rather slopping plateau at 2.0 V is observed. In the 2nd cycle, the short plateau at 2.4 V completely disappears, indicating that Li_2S_x is not stable in the electrolyte with carbonate solvents and $LiPF_6$. Zhang has reported that polysulfides can react with $LiPF_6$, resulting in rapid capacity fading of sulfur cathode in carbonate-based electrolyte.[35] The long plateau at 1.6 V shifts to a slopping plateau centered at 1.7 V owing to the release of strain/stress in C/S composite in the first cycle. After 100 cycles, the strain/stress of C/S composite is completely absorbed, and the slopping plateau shifts to 1.8 V, which is the intrinsic reaction potential for the lithiation of short-chain sulfur molecules. The corresponding delithiation plateau is

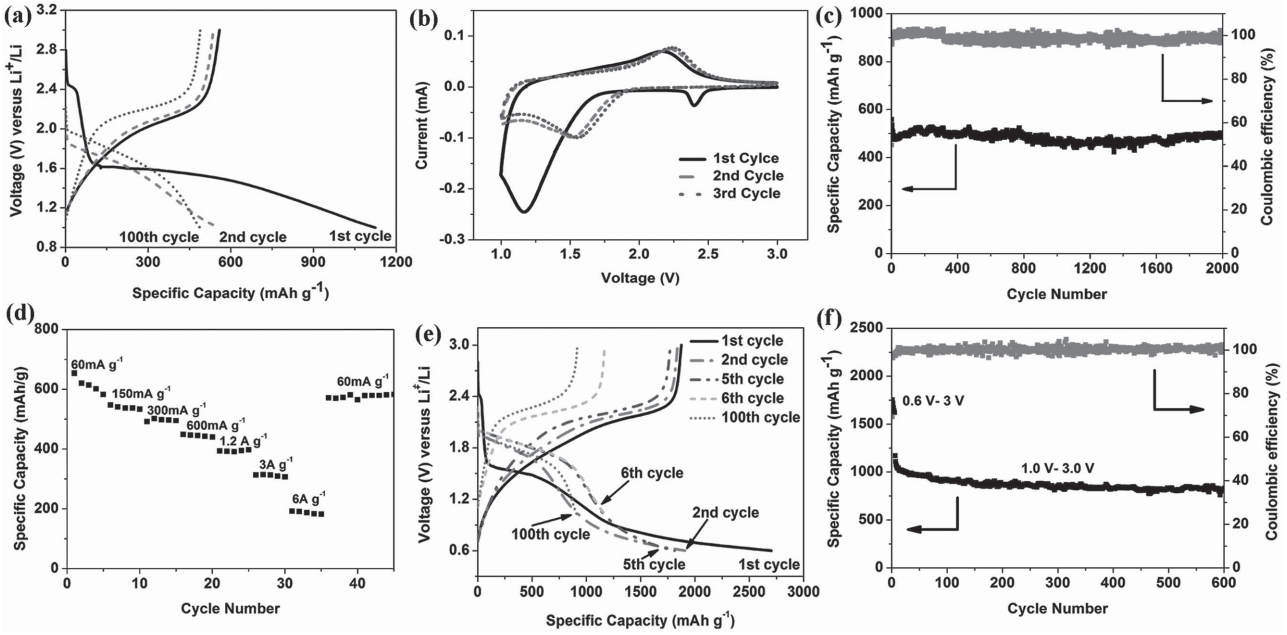

Figure 3. Electrochemical performance of oxygen-stabilized C/S composites. a) The galvanostatic charge–discharge curves between 1.0 and 3.0 V versus Li/Li^+; b) cyclic voltammograms at 0.1 mV s^{-1} in the potential window from 1.0 to 3.0 V versus Li/Li^+; c) delithiation capacity and coulombic efficiency versus cycle number at the current density of 150 mA g^{-1}; d) rate performance at various C-rates; e) the galvanostatic charge–discharge curves between 0.6 and 3.0 V in initial 5 cycles and between 1.0 and 3.0 V after 5 cycles; f) delithiation capacity and coulombic efficiency versus cycle number at the current density of 150 mA g^{-1} in the cutoff window from 0.6 to 3.0 V in initial 5 cycles and from 1.0 to 3.0 V after 5 cycles.

centered at 2.2 V after 100 cycles. Cyclic voltammograms in Figure 3b show that there are two cathodic peaks at 2.4 and 1.2 V and one anodic peak at 2.2 V in the first cycle, which coincide with galvanostatic tests. In the subsequent cycles, the cathodic peak at 2.4 V disappears, and both cathodic peak at 1.2 V and anodic peak at 2.2 V shift to positive values, which is consistent with charge/dicharge behavior in Figure 3a. The oxygen-stabilized C/S composites maintain a reversible capacity of 508 mAh/(g of S) at a current density of 150 mA g^{-1} for 2000 cycles with a Coulombic efficiency close to 100% (Figure 3c); however, poor electrochemical performance was demonstrated by the same composite in LiTFSI-DOL/DME, which is a more typical electrolyte used in literature (Figure S3, Supporting Information). This anomaly is consistent with the earlier report that a unique interphase can only be formed in carbonate-based electrolytes.[36] An excellent rate capability is also achieved by the composites, as indicated by Figure 3d. When current density increases from 60 mA g^{-1} to 6 A g^{-1}, the reversible capacity remains at 180 mAh/(g of S), which is over 30% of its initial capacity (580 mAh/(g of S)). After current density returns to 60 mA g^{-1}, the reversible capacity recovers its initial level without any kinetic delay.

Despite the excellent cycling stability and rate capability, the low reversible capacity of 508 mAh g^{-1} at a current density of 150 mA g^{-1} suggests that only part of the confined sulfur participates in the cell reaction and hence falls short of the promise of sulfur-based cathode. To liberate more sulfur that is harnessed by oxygen functionalities, we subjected the cathode to a prelithiation process down to the potential of 0.6 V, in the hope that electrochemical reduction could break the strong interaction between sulfur and oxygen. The consequence of this deep lithiation is the release of extra sulfur species that are originally immobilized by oxygen and their subsequent electrochemical activity. As shown in Figure 3e,f, the first five cycles are conducted between 0.6 and 3.0 V. There are three plateaus observed at 2.4, 1.6, and 0.7 V during the 1st lithiation, while only one plateau centered at 2.0 V is observed during the delithiation immediately thereafter. In the second cycle, the plateau at 2.4 V disappears, while the plateau at 1.6 V shifts to 1.8 V, and the plateau at 0.7 V becomes shorter. In the fifth cycle, the plateau at 0.7 V almost disappears, while the plateau at 1.8 V shifts to 1.9 V and becomes much longer than that in the second cycle. This dynamic change in the voltage profiles reflects that more and more sulfur is released in each cycle from the oxygen immobilization and then becomes available for the electrochemical reactions. After normal cycling protocol is resumed between 1.0 and 3.0 V starting at the 6th cycle, the newly increased capacity remains at 1170 mAh/(g of S), which is much higher than the delithiation capacity in Figure 3a,c, and this capacity rapidly stabilizes to 820 mAh/(g of S), which is retained for 600 cycles with negligible fadings at a Coulombic efficiency close to 100%. To confirm the origin of such extra capacity incurred by prelithiation, a blank test was conducted using carbonized neat PTCDA without sulfur by prelithiating it in the range of 0.6–3.0 V (Figure S4, Supporting Information), where a reversible capacity of only ≈60 mAh g^{-1} was observed, probably contributed by Li^+-intercalation into the graphitic portion of the carbon host as well as the surface non-Faradaic processes. Apparently, the extra capacity of >1000 mAh/(g of S) is not contributed by the carbon host itself.

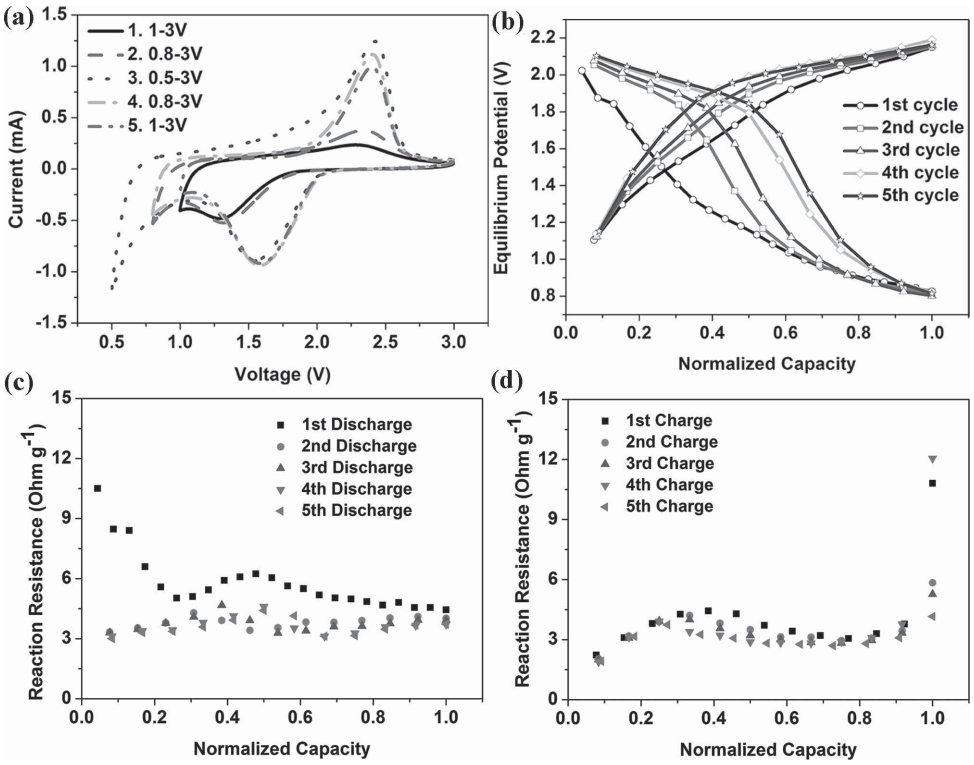

Figure 4. a) Cyclic voltammograms of oxygen-stabilized C/S composites in different potential windows versus Li/Li^+. b) Equilibrium potential versus normalized capacity during GITT measurement. Reaction resistance of oxygen stabilized C/S composites during GITT measurement from c) 1st discharge to 5th discharge and d) from 1st charge to 5th charge. Note: Current density was calculated based of the total weight of oxygen stabilized C/S composite. The charge/discharge capacity was normalized by dividing the discharge capacity.

2.3. Activation Mechanism of Prelithiation

To understand the activation mechanism of oxygen-stabilized C/S composites in different potential windows, cyclic voltammetry (CV) and galvanostatic intermittent titration technique (GITT) are carried out. **Figure 4**a shows the cyclic voltammograms of the composite in different potential windows at a scan rate of 0.5 mV s^{-1}. The cell is initially cycled from 1.0 to 3.0 V for two cycles, and then the potential window is widened from 0.8 to 3.0 V for another two cycles, followed by an even wider potential window from 0.5 to 3.0 V for five cycles with the purpose to fully lithiate S-species in the composite. After that, narrow window from 0.8 to 3.0 V is resumed for two cycles and then from 1.0 to 3.0 V for two cycles. Cyclic voltammograms of the last cycle in each potential window are displayed in Figure 4a. With the discharge potential changed from 1.0 to 0.8 V, and then to 0.5 V, the intensity of redox peaks becomes stronger with each cycle, consistent with the charge/discharge plateaus in Figure 3e that more S is released from carbon host upon deep discharging. The sharp rise of cathodic peaks at the end of each cathodic scan should be responsible for the formation of solid electrolyte interphase (SEI) layer and the continuous lithiation of sulfur-species immobilized by oxygen in the carbon host. With lower cut-off limit reverts to 0.8 and 1.0 V, the intensity of redox peaks becomes a little weaker due to the narrowed potential window, but it is much stronger than that of initial scan, indicating that extra sulfur has indeed been liberated from the carbon host during the deep lithiation process. The deeper the discharge, the more sulfur will be released. When the discharge potential is maintained at 0.5 V, the released sulfur in each cycle gradually reduces as demonstrated in Figure S5 (Supporting Information). Figure S5a (Supporting Information) shows that with a lower cutoff limit of 0.5 V, the sharp CV peak at the end of cathodic scan becomes weaker, while the intensity of redox peaks at 1.7 and 2.3 V increases from the 1st scan to the 30th scan. The voltage profiles in Figure S5b (Supporting Information) also confirm that the slopping plateau below 1.0 V becomes shorter, but the slopping plateau centered at 1.7 V becomes longer upon cycling, further confirming that deep discharging to 0.5 V can release more sulfur from carbon host. The equilibrium potential during lithiation/delithiation process is evaluated by GITT (Figure S6, Supporting Information). The oxygen-stabilized C/S electrode is lithiated/delithiated by a series of constant current pulse of 150 mA g^{-1} with an equal duration period of 1 h, and then rested for 12 h to reach the equilibrium potential after each current pulse. The colored symbol lines in Figure 4b represent the equilibrium open circuit potentials (OCP). Upon lithiation/delithiation cycles from 0.5 to 3.0 V, the equilibrium potential shifts upward. The slopping potential line changes into a plateau center at 1.7 V at the expense of reducing the slopping plateau below 1.0 V. More importantly, the lithiation/delithiation equilibrium OCP plateaus centered at 2.0 V are extended and shifted to positive values upon cycling, while the equilibrium plateau centered at 0.9 V becomes shorter with each cycle, consistent with the changes of voltage plateaus in

Figure 3e. The equilibrium potential curves of C/S composite change upon cycling, demonstrating that the deep lithiation process has changed the thermodynamics of C/S composite instead of kinetics. This fundamental change is due to the generation of new sulfur species produced by the reaction between Li^+ and oxygen-stabilized sulfur. The reaction resistance of C/S electrode during lithiation/delithiation process is calculated by dividing the overpotential with pulse current amplitude, as shown in Figure 4 c and 4d. Compared to the subsequent charge/discharge cycles, the reaction resistance in the 1st lithiation process is the largest, reflecting the largest strain/stress induced by the strong interaction and physical encapsulation of sulfur with oxygen-rich carbon matrix. The reaction resistance slightly decreases after 50% of lithiation, while the reaction resistance remarkably increases at the end of delithiation. The difference of reaction resistance during lithiation/delithation may be attributed to the electrical contact resistance change caused by the volume expansion/shrinkage during lithiation/delithiation process. Hence, both CV and GITT results confirm that prelithiating the composite at low potentials liberates sulfur species by changing their chemical valence states.

Electrochemical impedance spectroscopy is also used to monitor the impedance evolution upon cycling. The depressed semi-circle in the high frequency area represents interphasial resistance, including contact resistance of the composite particles, SEI layer, and charge transfer resistance, while the low frequency line stands for ion diffusion resistance in the composite particles. As shown in **Figure 5**, the interphasial resistances is ≈250 ohm for the fresh cell, while it increases to ≈700 ohm once discharged to 1.5 V, due to the lithiation of sulfur in the composite. When the discharge lower limit becomes 1.0 V, two depressed semicircles can be observed, and the interphasial resistance increases to ≈900 ohm, owing to the growth of SEI layer and further lithiation of sulfur in the composite. The first semicircle should represent the sum resistance of SEI layer and particle-to-particle resistance for the composite, while the second semi-circle stands for the charge transfer resistance. When the cell is further discharged to 0.6 V, the interphasial resistance decreases to 720 ohm. Though the resistance of SEI layer increases upon further discharging, contact resistance of the composite particles decreases due to the volume expansion, and more S is released by the lithiation process so that more active sites for sulfur and lithium ions are available, which helps reduce the charge transfer resistance. After the cell is charged to 3.0 V, the original value of ≈250 Ohm interphasial resistance was restored, representing an ideal state of both excellent conductivity and good integrity of the electrode. In the following five cycles, the interphasial resistance maintains this initial value, ensuring the excellent cycling stability of the sulfur-based cathode.

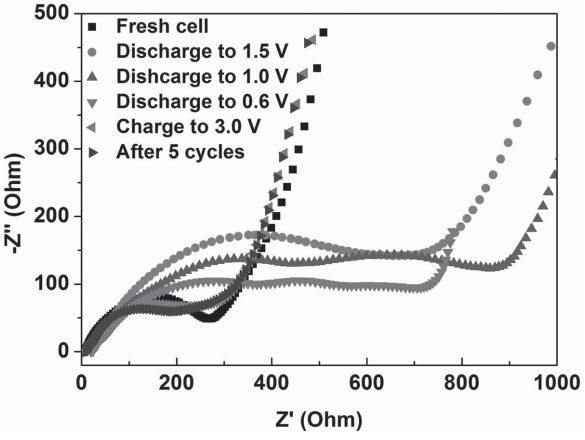

Figure 5. Impedance analysis for oxygen stabilized C/S cell before test and during discharge to 0.6 V and charge to 3.0 V.

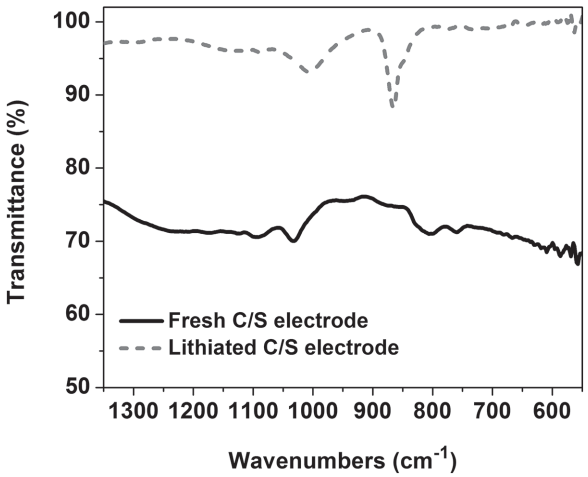

Figure 6. FTIR spectra for fresh C/S electrode and lithiated C/S electrode.

Fourier transform infrared spectroscopy (FTIR) is carried out to characterize the chemical bond between S and O in C/S electrode before and after deep discharge. It is very difficult to validate the disappearance of S–O bond after deep discharge because new S–O species will be formed at a deep discharge due to the formation of SEI, which cannot be removed by sputtering since SEI penetrates into the entire porous structure of C/S electrode. To avoid such interference, we directly react the C/S composite electrode with lithium metal in absence of any electrolyte by pressing a lithium sheet onto the C/S thin film electrode for two days to mimic the deep discharge, followed by FTIR. The FTIR spectrum of C/S electrode after deep chemical lithiation is compared to the pristine C/S electrode. Examination of the FTIR spectra of the fresh C/S composite shown in **Figure 6** indicates presence of two peaks at 1032 cm^{-1} and 805 cm^{-1} that are assigned to C–O bond stretching and aromatic ring breathing mode for C/S composite electrode with –O–S– bonds formed, respectively. The peak at 805 cm^{-1}, attributed to C/S composite with S–O bond, disappears after deep chemical lithiation due to S–O bond dissociation, while the C–O peak at 1032 cm^{-1} shifts to 1004 cm^{-1} due to $Li^+ \cdots O$ bond formation. These peak assignments are confirmed by density functional theory (DFT) calculations performed using PTCDA and its complexes with Li^+, LiS_4^-, Li_2S_4, and S_8 as representative model system as shown in Figures S7–S10 (Supporting Information). The disappearance of S–O bond in the FTIR spectrum of the lithiated C/S electrode is attributed to the activation of oxygen-stabilized S by the reaction between lithium ions and S during deep discharging, which disassociates the S–O bond. The FTIR spectra for the C/S electrode before and after lithiation proved

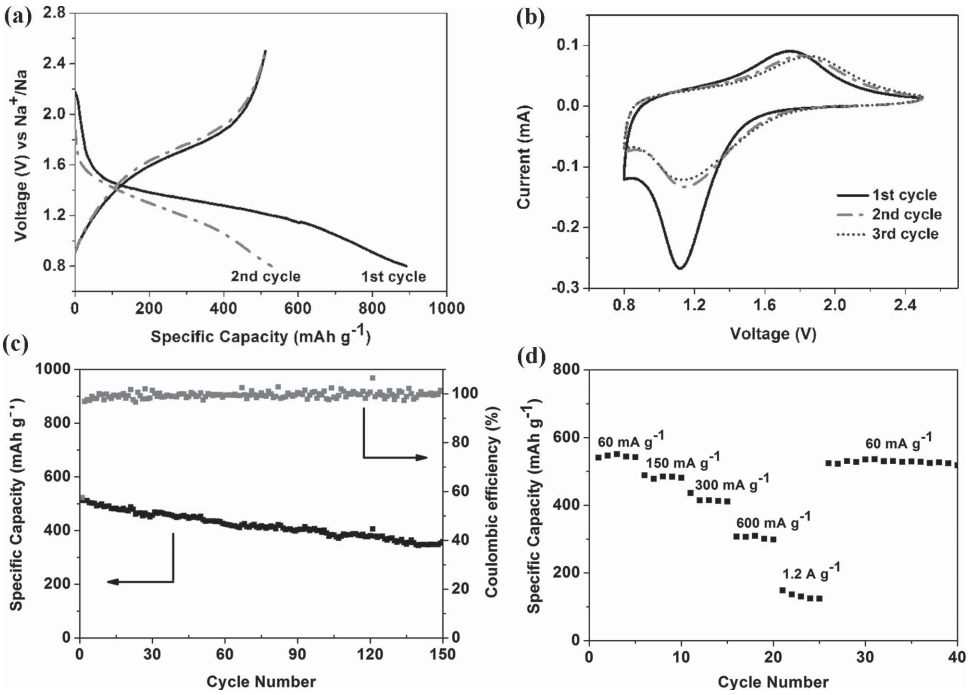

Figure 7. Electrochemical performance of oxygen-stabilized C/S composites. a) The galvanostatic charge–discharge curves between 0.8 and 2.5 V versus Na/Na^+. b) Cyclic voltammograms at 0.1 mV s^{-1} in the potential window from 0.8 to 2.5 V versus Na/Na^+. c) Desodiation capacity and coulombic efficiency versus cycle number at the current density of 150 mA g^{-1}. d) Rate performance at various C-rates.

our hypothesis that the oxygen-stabilized sulfur can be released after deep discharging.

The morphology change of lithium metal after long-term cycling was investigated by SEM. As shown in Figure S11 (Supporting Information), smooth surface with holes between Li was observed after continuous charge/discharge process. The microsized pores and dents can be clearly observed on the surface of lithium metal due to the dissolution of lithium ions in the electrolyte during the discharge process.

Besides the cell chemistry coupled with Li anode, the obtained oxygen-stabilized C/S composites are also coupled with Na anode. The electrochemical performance of the composites is measured between 0.8 and 2.5 V versus Na/Na^+. As shown in **Figure 7**a, the sodiation and desodiation plateaus are centered at 1.4 and 1.8 V, respectively, which are 0.4 V lower than the Li counterparts. Cyclic voltammograms in Figure 7b confirm that there is only one pair of redox peaks at 1.15 and 1.7 V, respectively during sodiation/desodiation, revealing that the cell reaction consists of a one step mechanism between sulfur and Na in this composite. The oxygen-stabilized C/S composites deliver a reversible capacity of 500 mAh g^{-1} at the current density of 150 mA g^{-1} initially, which reduces to 400 mAh g^{-1} after 150 cycles, as shown in Figure 7c. The rate capability of the composite is also measured by increasing the current density every five cycles, as shown in Figure 7d, in which the desodiation capacity decreases from 550 to 130 mAh g^{-1}, when the current density increases by 20 times from 60 mA g^{-1} to 1.2 A g^{-1}. This combination of decent cycling stability and rate capability makes the electrochemical couple between Na and oxygen-stabilized C/S composite promising cell chemistry for Na/S batteries.

3. Conclusion

The oxygen-stabilized C/S composites are synthesized by annealing the mixture of sulfur and perylene-3,4,9,10-tetracarboxylic dianhydride in a sealed vacuum glass tube. The resulting composites exhibit superior electrochemical performance for both Li and Na cells. In the Li cell, a reversible capacity of 508 mAh g^{-1} is maintained in carbonate-based electrolyte for 2000 cycles when cycled between 1.0 and 3.0 V. Furthermore, it is discovered that extra reversible capacity could be obtained if prelithiating the composite at low potentials (0.6 V), as evidenced by the stably delivered 820 mAh/(g of S) for over 600 cycles and a Coulombic efficiency close to 100%. Based on spectroscopic studies, we attributed the extra capacity to the sulfur-species liberated by the prelithiation from their strong interaction with oxygen functionalities in the carbon host. Similar excellent electrochemical performance is also achieved when the C/S composite is coupled with Na anode, where a reversible capacity of 400 mAh g^{-1} is maintained for 150 cycles. Therefore, the oxygen-stabilized C/S composites make promising sulfur-cathode materials for both Li-S and Na-S batteries.

4. Experimental Section

Synthesis of C/S Composites: All chemicals were purchased from Sigma-Aldrich and used as received. Sulfur and perylene-3,4,9,10-tetracarboxylic dianhydride were mixed with a ratio of 1.5:1 by weight and sealed in a glass tube under vacuum. The sealed glass tube was annealed in an oven at 600 °C for 3 h, and it was cooled to room temperature in 24 h. Oxygen-stabilized C/S composites were collected as black powder.

Material Characterizations: SEM images were taken by Hitachi SU-70 analytical ultrahigh resolution SEM (Japan). TEM images were taken by JEOL (Japan) 2100F field emission TEM. TGA was carried out using a thermogravimetric analyzer (TA Instruments, USA) with a heating rate of 10 °C min^{-1} in argon. XRD pattern was recorded by Bruker Smart1000 (Bruker AXS Inc., USA) using Cu Kα radiation. Raman measurements were performed on a Horiba Jobin Yvon Labram Aramis using a 532 nm diode-pumped solid-state laser, attenuated to give ≈900 μW power at the sample surface. The XPS analysis was performed on a high sensitivity Kratos AXIS 165 X-ray photoelectron spectrometer using monochronic Al Kα radiation. The elemental analysis was performed by ALS Environmental Company. FTIR was recorded by NEXUS 670 FT-IR Instrument.

Electrochemical Measurements: The oxygen stabilized C/S composites were mixed with carbon black and sodium alginate binder to form a slurry at the weight ratio of 80:10:10. The electrode was prepared by casting the slurry onto aluminum foil using a doctor blade and dried in a vacuum oven at 60 °C overnight. The slurry coated on aluminum foil was punched into circular electrodes with an area mass loading of 1.2 mg cm^{-2}. Coin cells for lithium sulfur batteries were assembled with lithium foil as the counter electrode, 1 M $LiPF_6$ in a mixture of ethylene carbonate/diethyl carbonate (EC/DEC, 1:1 by volume) and Celgard3501 (Celgard, LLC Corp., USA) as the separator. Coin cells for sodium sulfur batteries were assembled with sodium metal as the counter electrode, 1 M $NaClO_4$ in a mixture of ethylene carbonate/dimethyl carbonate (EC/DMC, 1:1 by volume) and Celgard3501 (Celgard, LLC Corp., USA) as the separator. Electrochemical performance was tested using Arbin battery test station (BT2000, Arbin Instruments, USA). Capacity was calculated on the basis of the weight of sulfur in C/S composites. Cyclic voltammograms were recorded using Gamry Reference 3000 Potentiostat/Galvanostat/ZRA with a scan rate of 0.1 mV s^{-1}.

Supporting Information

Supporting Information is available from the Wiley Online Library or from the author.

Acknowledgements

This work was supported by the Army Research Office under Contract No. W911NF10200. The authors acknowledge the support of the Maryland Nano Center and its NispLab. The NispLab is supported in part by the NSF as a MRSEC Shared Experimental Facility. The authors acknowledge Dr. Cynthia Lundgren and Dr. Karen Gaskell for the technique support.
Note: Figure 1 was amended on February 1, 2016.
Received: September 15, 2015
Revised: November 4, 2015
Published online: December 10, 2015

[1] B. Scrosati, J. Hassoun, Y.-K. Sun, *Energy Environ. Sci.* **2011**, *4*, 3287.
[2] J. B. Goodenough, Y. Kim, *Chem. Mater.* **2010**, *22*, 587.
[3] B. L. Ellis, K. T. Lee, L. F. Nazar, *Chem. Mater.* **2010**, *22*, 691.
[4] B. Kang, G. Ceder, *Nature* **2009**, *458*, 190.
[5] Y. Zhu, Y. Xu, Y. Liu, C. Luo, C. Wang, *Nanoscale* **2013**, *5*, 780.
[6] S. J. Shi, Z. R. Lou, T. F. Xia, X. L. Wang, C. D. Gu, J. P. Tu, *J. Power Sources* **2014**, *257*, 198.
[7] F. Wu, N. Li, Y. Su, L. Zhang, L. Bao, J. Wang, L. Chen, Y. Zheng, L. Dai, J. Peng, S. Chen, *Nano Lett.* **2014**, *14*, 3550.
[8] U. Kasavajjula, C. Wang, A. J. Appleby, *J. Power Sources* **2007**, *163*, 1003.
[9] C. Wang, H. Wu, Z. Chen, M. T. McDowell, Y. Cui, Z. Bao, *Nat. Chem.* **2013**, *5*, 1042.
[10] X. Chen, J. Guo, K. Gerasopoulos, A. Langrock, A. Brown, R. Ghodssi, J. N. Culver, C. Wang, *J. Power Sources* **2012**, *211*, 129.
[11] S. Zheng, F. Yi, Z. Li, Y. Zhu, Y. Xu, C. Luo, J. Yang, C. Wang, *Adv. Funct. Mater.* **2014**, *24*, 4156.
[12] X. Ji, K. T. Lee, L. F. Nazar, *Nat. Mater.* **2009**, *8*, 500.
[13] P. G. Bruce, S. A. Freunberger, L. J. Hardwick, J. M. Tarascon, *Nat. Mater.* **2012**, *11*, 19.
[14] Y. Zhao, W. Wu, J. Li, Z. Xu, L. Guan, *Adv. Mater.* **2014**, *26*, 5113.
[15] C. Luo, Y. Zhu, Y. Wen, J. Wang, C. Wang, *Adv. Funct. Mater.* **2014**, *24*, 4082.
[16] A. Manthiram, Y. Fu, Y.-S. Su, *Acc. Chem. Res.* **2013**, *46*, 1125.
[17] Z. W. Seh, W. Li, J. J. Cha, G. Zheng, Y. Yang, M. T. McDowell, P. C. Hsu, Y. Cui, *Nat. Commun.* **2013**, *4*, 1331.
[18] L. Suo, Y. S. Hu, H. Li, M. Armand, L. Chen, *Nat. Commun.* **2013**, *4*, 1481.
[19] J. Gao, M. A. Lowe, Y. Kiya, H. D. Abruña, *J. Phys. Chem. C* **2011**, *115*, 25132.
[20] J. Schuster, G. He, B. Mandlmeier, T. Yim, K. T. Lee, T. Bein, L. F. Nazar, *Angew. Chem. Int. Ed.* **2012**, *51*, 3591.
[21] J. Guo, Y. Xu, C. Wang, *Nano Lett.* **2011**, *11*, 4288.
[22] H. Wang, Y. Yang, Y. Liang, J. T. Robinson, Y. Li, A. Jackson, Y. Cui, H. Dai, *Nano Lett.* **2011**, *11*, 2644.
[23] M. Q. Zhao, Q. Zhang, J. Q. Huang, G. L. Tian, J. Q. Nie, H. J. Peng, F. Wei, *Nat. Commun.* **2014**, *5*, 3410.
[24] L. Ji, M. Rao, H. Zheng, L. Zhang, Y. Li, W. Duan, J. Guo, E. J. Cairns, Y. Zhang, *J. Am. Chem. Soc.* **2011**, *133*, 18522.
[25] L. Ji, M. Rao, S. Aloni, L. Wang, E. J. Cairns, Y. Zhang, *Energy Environ. Sci.* **2011**, *4*, 5053.
[26] N. Jayaprakash, J. Shen, S. S. Moganty, A. Corona, L. A. Archer, *Angew. Chem. Int. Ed.* **2011**, *50*, 5904.
[27] R. Elazari, G. Salitra, A. Garsuch, A. Panchenko, D. Aurbach, *Adv. Mater.* **2011**, *23*, 5641.
[28] X. Ji, S. Evers, R. Black, L. F. Nazar, *Nat. Commun.* **2011**, *2*, 325.
[29] J. Guo, Z. Yang, Y. Yu, H. D. Abruna, L. A. Archer, *J. Am. Chem. Soc.* **2013**, *135*, 763.
[30] J. Wang, J. Yang, C. Wan, K. Du, J. Xie, N. Xu, *Adv. Funct. Mater.* **2003**, *13*, 487.
[31] L. Yin, J. Wang, F. Lin, J. Yang, Y. Nuli, *Energy Environ. Sci.* **2012**, *5*, 6966.
[32] S. Xin, L. Gu, N. H. Zhao, Y. X. Yin, L. J. Zhou, Y. G. Guo, L. J. Wan, *J. Am. Chem. Soc.* **2012**, *134*, 18510.
[33] L. Q. Lu, L. J. Lu, Y. Wang, *J. Mater. Chem. A* **2013**, *1*, 9173.
[34] C. Nan, Z. Lin, H. Liao, M. K. Song, Y. Li, E. J. Cairns, *J. Am. Chem. Soc.* **2014**, *136*, 4659.
[35] S. S. Zhang, *J. Power Sources* **2013**, *231*, 153.
[36] Y. Xu, Y. Wen, Y. Zhu, K. Gaskell, K. A. Cychosz, B. Eichhorn, K. Xu, C. Wang, *Adv. Funct. Mater.* **2015**, *25*, 4312.